Compressive behavior of rigid polyurethane foams nanostructured with bacterial nanocellulose at low and intermediate strain rates

Leonel Matías Chiacchiarelli,[1,2] **Patricia Cerrutti**,[3] **Emmanuel A. Flores-Johnson**[4]

[1]Instituto de Tecnología de Polímeros y Nanotecnología (ITPN), CONICET-UBA, Avda. Gral. Las Heras 2214, Buenos Aires, Argentina
[2]Departamento de Ingeniería Mecánica, Instituto Tecnológico de Buenos Aires, Avenue E. Madero 399, Buenos Aires, Argentina
[3]Departamento de Ingeniería Química, Facultad de Ingeniería, Universidad de Buenos Aires, Buenos Aires, Argentina
[4]CONACYT – Unidad de Materiales, Centro de Investigacion Cientifica de Yucatan, Calle 43, No. 130, Col. Chuburna de Hidalgo, Merida 97205, Yucatan, Mexico
Correspondence to: L. M. Chiacchiarelli (E-mail: lchiacchiarelli@itba.edu.ar)

ABSTRACT: Nanocellulose reinforced foams are lightweight with improved mechanical properties; however, the strain-rate effect on their mechanical response is not yet fully understood. In this work, rigid polyurethane foams (PUFs) nanostructured with bacterial nanocellulose at 0.2 wt % (BNCF) and without it (PUF) are synthesized and subjected to compression tests at different strain rates. The BNC acts as a nucleation agent, reducing the cell size but maintaining a similar apparent density of 40.4 ± 3.3 kg m^{-3}. Both BNCF and PUF exhibit strain-rate effect on yield stress and densification strain. The BNCF exhibits localized progressive crushing and reduced friability, causing a remarkable recovery in the transverse direction. Numerical simulations show that functionally graded foams subjected to impact could be designed using different layers of PUF and BNCF to vary energy absorption and acceleration rate. The results presented herein warrant further research of the mechanical properties of nanostructured foams for impact applications.

KEYWORDS: biopolymers and renewable polymers; foams; mechanical properties; nanostructured polymers; theory and modeling

INTRODUCTION

Rigid polyurethane foams (RPUFs) are widely used in a variety of industrial applications such as thermal insulation and construction of lightweight materials. Both the low density and high insulation value of RPUFs are excellent properties for the fabrication of industrialized sandwich panels[1,2] to construct commercial, residential, and industrial buildings.[3,4] Another relevant property of RPUFs is their excellent energy absorption capability.[5] Such property is of utmost importance for the development of materials that can absorb energy under impact scenarios, where protection of the human body is vital. For example, within the automotive industry, the use of paddings with a high level of crashworthiness is a key aspect to improve the security standards of domestic vehicles.[6,7] Other suitable applications of RPUFs include helmets,[8] impact resistant work gloves, cushioning,[9] insulation,[10] and packaging.[11,12]

The development of polymer nanocomposites has produced a new class of materials with superior mechanical,[13] thermal,[14] and transport properties.[15] These properties depend on several factors, such as the polymer synthesis method,[16,17] the mixing process,[18] and the nanoreinforcement.[13] In this regard, Cordero *et al.*[19] found that the incorporation of a small amount of nanocellulose obtained by hydrolysis can have a substantial improvement of the mechanical properties of polyurethane foams (PUFs) synthesized from castor oil. In a recent study by Gimenez *et al.*,[20] it was found that the development of RPUFs from bacterial nanocellulose (BNC) may result in a relevant increase in its specific mechanical properties. Several studies[21,22] have also emphasized that the use of nanostructured foams[23,24] could improve the specific mechanical properties of the material.[25,26] In this regard, nanocellulose[27,28] is a promising candidate in the development of sustainable,[29,30] nontoxic,[31] and low density[32] RPUFs with enhanced mechanical properties.[33,34] Most of the aforementioned studies have been aimed at investigating the synthesis of the nanostructured RPUFs with little focus on the strain-rate dependence of the mechanical properties.

In order to develop materials for impact applications based on RPUFs, it is very important to know the evolution of the compressive stress–strain curves at different strain rates. In this regard, there have been several studies of the effect of strain rate on RPUFs.[35,36] The stress–strain curve of a RPUF under dynamic loading is similar to that of foams under quasi-static loading[37]; however, the peak stress is strain-rate sensitive and increases with the increase of strain rate.[38,39] For this reason, it is important to

study the stress–strain relationships at different strain rates for the development of impact resistant RPUFs. For example, for the design of the energy-absorbing layer in a polo helmet, it is more relevant to know the maximum stress of the plateau region than the total energy absorbed by the RPUF up to densification as high peak stresses will inevitably cause a severe trauma to the polo helmet user. In some impact applications, it is desirable that the impact energy is absorbed at specific rates in order to produce steady decelerations since large and fast decelerations may produce injuries.[40]

Another distinctive property of an RPUF is its anisotropy.[12] For the particular case of molded RPUFs, the cells are prone to align in a particular direction due to the anisotropic growth behavior caused by boundary conditions. In the case of open-molded RPUFs, it is common to find that cells are elongated in the growth direction when compared to the transverse direction.[19,20] This has an important effect on the mechanical properties. For example, the compressive strength in the growth direction can be as much as 50% higher than that in the transverse growth direction.[41] In contrast to the well-studied dynamic properties of RPUFs and other cellular materials,[42,43] there are limited studies on the dynamic properties of nanostructured RPUFs. Uddin *et al.*[44] studied the reinforcement of RPUFs with spherical TiO_2 and acicular carbon nanofiber. They found that both nanoparticles contributed to higher energy absorption and failure strength. Mohammed *et al.*[45] found that RPUFs reinforced with nanoclay up to 1 wt % exhibited improved mechanical properties. Other works have also studied the strain-rate effect[46] on the compression properties of RPUFs using short glass fibers,[47,48] hollow glass microspheres,[49] nanofillers,[50] and sandwich panels[51,52] using nanostructured foams.[53,54]

Although many studies have been performed to understand the properties of RPUFs reinforced with nanocellose,[55] most of those studies were conducted using nanocrystalline cellulose (CNC) obtained via hydrolysis.[56] Some recent investigations using BNC[57,58] have shown that BNC can be incorporated into solid polyurethane composites to improve the mechanical properties; however, the effect of incorporating BNC into RPUFs has barely been studied. In a recent study, quasi-static compressive strength of nanostructured RPUFs using BNC was reported[20]; however, the effect of strain rate on the dynamic compressive properties of this material was not studied. Based in the aforementioned literature and given the fact that there is limited knowledge concerning the dynamic behavior of nanostructured RPUFs with BNC, the objective of the present study is to investigate the strain-rate effect on the compression behavior of RPUFs nanostructured with BNC in different loading directions. The outcomes of this study could provide a new approach to improve the mechanical performance of functionally graded foams (FGFs) with tailored energy absorption properties for impact applications. In this work, the synthesis of RPUFs with BNC dispersed in the polyol at a very low concentration (0.2 wt %), using commercially available isocyanates and polyols, is reported. The compressive stress–strain behavior at different strain rates is studied for both the longitudinal (rise direction) and transverse directions. Finite element (FE) simulations were performed to study FGFs; the effect of using layers with the same density but different energy absorptions on the dynamic behavior of FGFs is reported.

EXPERIMENTAL

Raw Materials and Preparation of RPUFs

The RPUFs were synthesized using commercially available precursors. Methylene diphenyl diisocyanate (Suprasec 5005; Huntsman Corporation, Buenos Aires, Argentina) was used as received. The isocyanate group (NCO) content reported by the manufacturer (31.5%) was corroborated using the procedure described in the ASTM D2572 standard. This procedure was implemented before each experiment to ensure that relevant changes of the NCO number did not occur. A polyester polyol (Suprasec 18497; Huntsman Corporation) was used. Dimethylcyclohexylamine (Rubitherm LR18412; Huntsman Corporation) was employed as an amine catalyst. 1,1-Dichloro-1-fluoroethane (HCFC 141b) was used as the physical expansion agent. HCFC 141b is commonly used for slabstock RPUF formulations.[59] The formulation of the RPUF synthesized in this work consisted of 160 pbw of Suprasec 5005, 14 pbw of HCFC 141b, 3 pbw of LR18412, and 100 pbw of Suprasec 18497. It represents a typical formulation for a slabstock RPUFs.[11] RPUFs were prepared by the one-shot method[11] using the following procedure: First, all the components except the isocyanate were dispersed in the polyol (dispersion medium) using a homogenizer at 3500 rpm for 2 min. Second, the isocyanate was added to the mix, which was then poured into a cylindrical mold with an internal diameter of 70 mm, while being rapidly dispersed with a Cowles stirrer rotating at 2000 rpm for 30 s. A K type thermocouple coupled with an ultrasonic distance sensor (HC-sr05) was used to make *in situ* measurements of temperature and foam rise height. After the bun of 70 mm diameter and approximately 20 cm height was demolded, a CNC controlled band saw sliced the foam into pieces of 25 mm in thickness. Then, further CNC machining was implemented to obtain cubes with dimensions of $25 \times 25 \times 25$ mm^3 (this procedure was performed for the PUF and the BNCF samples). Subsequently, all samples were placed in an oven at 60 °C for 1 h. Finally, sample weight was measured using an analytical balance (Ohaus Adventurer) to obtain the apparent density.

BNC was produced by a strain of *Gluconacetobacter xylinus*, kindly provided by Dr. Luis Lelpi (Fundación Instituto Leloir, Buenos Aires, Argentina). The method to obtain BNC pellicles is described in detail elsewhere.[20] A brief description of this method is as follows: Static fermentations were carried on for 14 days in a Hestrin and Schramm medium modified by replacing D-glucose with an identical concentration of glycerol (Biopack) at 28 ± 1 °C, while maintaining a ratio "volume flask:volume medium" of 5:1. After BNC pellicles (mats) were obtained, they were rinsed with water to remove the culture medium and then boiled in 2% w/v NaOH solution for 1 h to eliminate bacterial cells from the cellulose matrix. BNC mats were neutralized with distilled water prior to fabrication of nanostructured foam. To obtain a nanostructured RPUF (BNCF), the BNC was dispersed in the polyol component following the "POLMIX" method.[60] Initially, the aqueous BNC mat was lyophilized using a Labconco FreeZone 2.5 equipment. Lyophilization is a key aspect to promote nanometric dispersion. Conventional drying procedures could produce BNC agglomerates, which may result in a loss of nanometric features and mechanical performance.[61] The procedure lasted for 72 h (vacuum of 0.02 mbar and temperature of −52 °C). After this procedure, a dry BNC mat was obtained, which was then triturated using a high shear mixing

blender to obtain BNC millimetric-size particles. Subsequently, those particles were inserted in the polyol and homogenized at 3500 rpm for three intervals of 2 min. Every precaution was taken to avoid temperature increase during the homogenization process. The BNC was mixed in the polyol for a total equivalent concentration of 0.2 wt % (which was 0.554 wt %). In other words, the total BNC concentration for the BNCF was 0.2 wt %, whereas the BNC concentration in the polyol was 0.554 wt %. Finally, the nanostructured polyol was formulated with the other components and the *in situ* foaming reaction proceeded as described above.

Microscopy

Scanning electron microscopy (SEM) analysis was conducted on a low vacuum scanning electron microscope JEOL JSM 6360. Specimens with dimensions of $20 \times 10 \times 3$ mm^3 cut from a foam sample were glued on copper grids and coated with gold for better electron conductivity. Images of the foam were used to determine the average size of foam cells in both longitudinal (rise) and transverse directions. Statistical analysis of cell size was undertaken using the commercial software ImageJ (v. 1.60; National Institutes Health, Bethesda, MD).

Compression Tests

Both quasi-static and intermediate strain-rate compression tests were performed on the foam samples. Both PUF and BNCF were cut into $25 \times 25 \times 25$ mm^3 cubes. Quasi-static compression tests were performed using a universal testing machine (Shimadzu AGS-X, Japan) equipped with a 1-kN load cell. Two different crosshead speeds were implemented, that is, 2.5 and 25 mm min^{-1}, which produced strain rates of ~0.0016 and ~0.016 s^{-1}, respectively. Intermediate strain-rate compression tests were conducted using a drop-weight impact tower, which was designed and built in-house (Figure 1). Specimens were placed on a steel plate and impacted using a steel cylindrical impactor [Figure 1(b)] with a diameter of 50 mm. The impactor was attached to a weight of 1.6 kg. A 50-kN load cell (Kistler 9333A) and a triaxial accelerometer (Slam Stick X) were attached to the impactor. The load cell was connected to a signal amplifier with a 180 kHz low-pass built-in electronic filter. Here, the measuring range of the load cell was adjusted according to the expected level of load to reduce signal noise. An impact velocity of 3.7 m s^{-1} was calculated according to the free-fall formula[62] for a drop height of 0.7 m. This, in turn, produced an initial strain rate of ~150 s^{-1}. It is noted that a constant strain rate is not achieved due to the deceleration of the impactor during foam compression.[63]

Compressive properties at quasi-static and low velocity impact conditions were measured for both longitudinal (parallel to rise direction) and transverse (perpendicular to rise direction) directions. For each direction, at least three specimens were measured. For the intermediate strain-rate compression tests, the force-time history from filtered load cell signal and the displacement-time history from accelerometer (obtained by double integration of the acceleration vs. time curve) were used to obtain the force-displacement curves. Subsequently, the stress–strain curves were calculated. A fast camera Sony Cyber-shot DSC-RX100 IV recording at 1000 frames per second was used to capture the specimen deformation.

EXPERIMENTAL RESULTS

Synthesis, *In Situ* Growth, and SEM Analysis of the PUF and BNCF

The rise height and *in situ* temperature during the synthesis of the PUF and the BNCF are reported in Figure 2. For the PUF, the inhibition time after mixing both components lasted approximately 173 s. After this time, a steep rise in the foam was attained, which lasted on average 50 s and yielded a final height of 18.1 cm. On the other hand, the BNCF had a larger inhibition time of around 342 s, and a final height of 17.0 cm was measured after approximately 50 s. The *in situ* temperature measurements are reported in Figure 2(b). For the case of the PUF, the end of the inhibition period and the beginning of the temperature rising due to polymerization and foaming coincided with the initiation of foam growth, as expected. The main difference between the PUF and the BNCF was associated with the maximum temperature achieved after the reaction. For the PUF, this temperature was slightly lower (3.5 ± 0.8 °C) than that of the BNCF. From these results, it can be concluded that

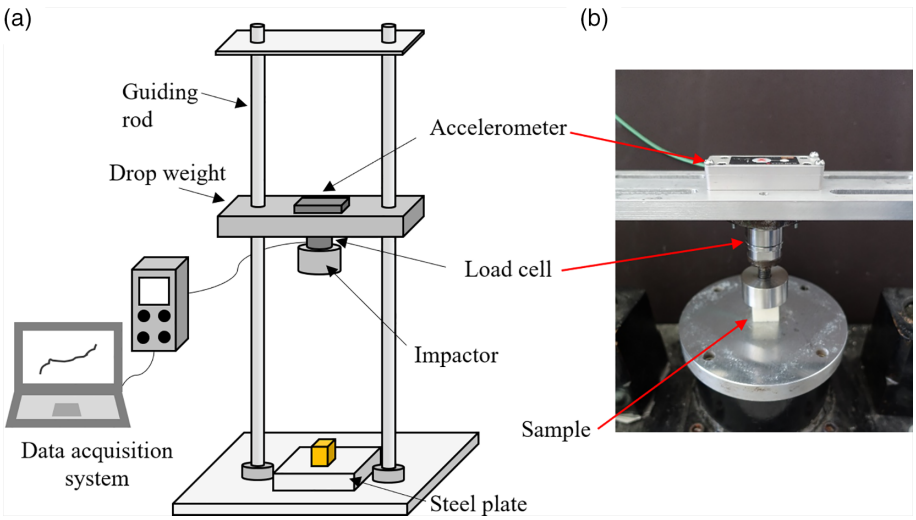

Figure 1. Drop-weight impact tower: (a) setup and (b) image of specimen on steel plate before impact test. [Color figure can be viewed at wileyonlinelibrary.com]

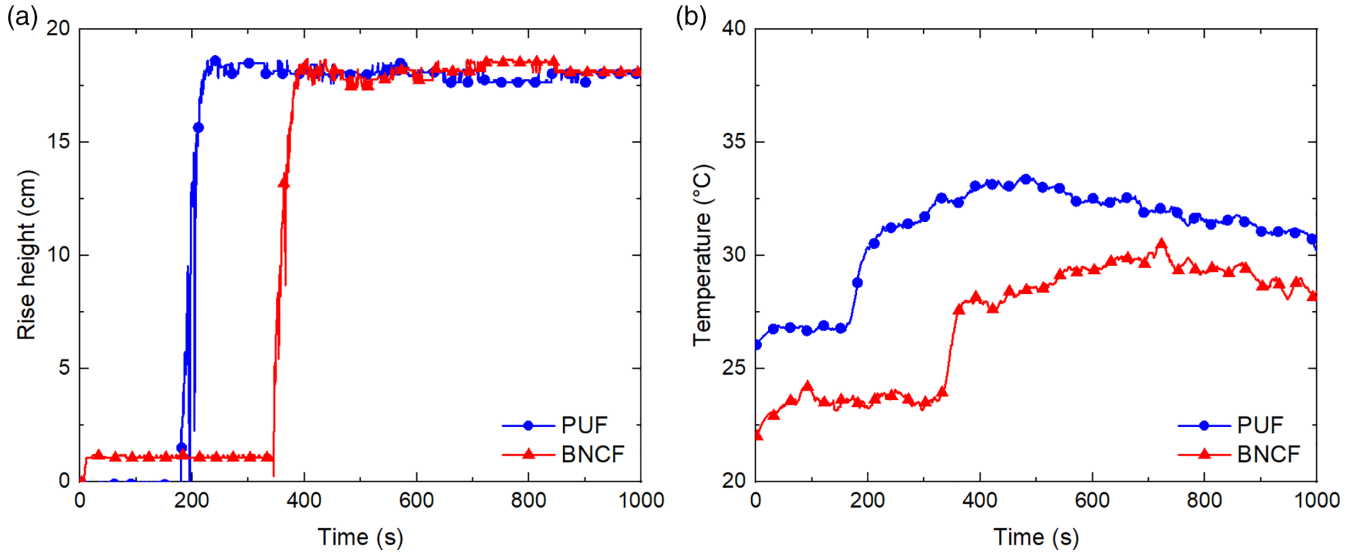

Figure 2. (a) Rise height of the foam as a function of the reaction time for the PUF and the BNCF. (b) *In situ* temperature for the PUF and the BNCF. [Color figure can be viewed at wileyonlinelibrary.com]

the BNC acted as an inhibitor. As already reported by previous studies,[19,20] the BNC can induce relevant changes of the microstructure of a RPUF and those changes can be deduced from *in situ* temperature rise measurements. For example, it is known that during rise, there is a competition of the gelling and blowing reactions and the outcome of this competition determines the microstructure of the RPUF.[20] The BNC increased the inhibition time and slightly decreased the exotherm of the reaction. In other words, the BNC acted as a nanofiller, changing the microstructure of the RPUF without inducing a significant change in its chemical nature.

The measured apparent density of the PUF was 41.2 ± 1.2 kg m^{-3}, whereas for the BNCF the average value was 40.4 ± 3.3 kg m^{-3}. Notwithstanding that both densities can be considered very similar from a practical point of view, the standard deviation of the BNCF is more than double than that of the PUF. These results suggest that the incorporation of BNC into the foam resulted in a slightly more heterogeneous structure. SEM images of the microstructure of both PUF and BNCF are shown in Figure 3. It can be seen in Figure 3(a) that the PUF had an asymmetric growth and the cells are slightly elongated in the direction of growth. This observation is explained by the fact that the foam was molded into solid blocks. Figure 3(b) shows the cross section of a single strut of the PUF, which exhibits a smooth surface. This indicates that the fracture of the strut occurred without the creation of additional fracture planes. From the statistical analysis of the cell size of PUF, it was obtained that the cell size parallel to the growth direction was 615 ± 106 μm, whereas the cell size in the perpendicular direction was 369 ± 59 μm. On the other hand, the cell size of the BNCF [Figure 3(c)] showed a reduced size in both directions, that is, the cell size in the longitudinal and transverse directions was 449 ± 143 μm and 242 ± 61 μm, respectively. This decrease of cell size has been observed for other nanostructured RPUFs[64] and it is associated with the BNC acting as a nucleation agent.[19] It is noted that the role of BNC in the RPUF microstructure is highly influenced by isocyanate index and isocyanate number.[19] Figure 3(d) shows the cross section of a single strut of the BNCF. It can be seen in Figure 3(d) a rougher surface when compared to the surface of the PUF strut. This indicates that in the BNCF, additional fracture planes were created when the cells fractured.[20]

It can also be seen in Figure 3(c) that the BNC caused a slight deviation of cell orientation with respect to the rise direction of roughly ~10–15°. This may be the result of the BNC acting as a thixotropic reinforcement, which causes a delayed change in viscosity due to the *in situ* temperature increase during rise.[12]

Quasi-Static Compression and Low Velocity Impact Test of the PUF and BNCF

Typical true stress–true strain curves from compression tests performed at different strain rates are shown in Figure 4. In the case of the PUF and BNCF in the longitudinal direction (rise direction), the evolution of the stress–strain curves for all strain rates followed three stages, that is, an initial linear-elastic stage, a second stage in which the stress is roughly constant (plateau regime) and a third stage associated with a substantial increase of stress with further increase of the compressive strain, which is usually denoted as the densification stage.[65] On the other hand, for all strain rates in the transverse direction, it is observed that for the BNCF after the elastic regime, there is no plateau stress, and strain hardening is observed. For the PUF in the transverse direction, it is observed that there is a plateau regime up to ~25% strain, which is followed by strain hardening. For both PUF and BNCF, the yield stress is higher in the longitudinal direction when compared to the transverse direction. This is associated with the shape of the cells (anisotropy of the foams) (Figure 3).[66] Table I shows the average values of elastic modulus E, yield stress σ_y, yield strain ε_y, and densification strain ε_d, which were measured from quasi-static uniaxial compression curves for all the materials. σ_y and ε_y were measured as described in Li *et al.*[67] In this methodology, for a stress–strain response where yield is followed by softening, σ_y refers to the initial peak stress. For a strain-hardening response, σ_y is determined from the intersection of two tangents, one to the initial elastic part,

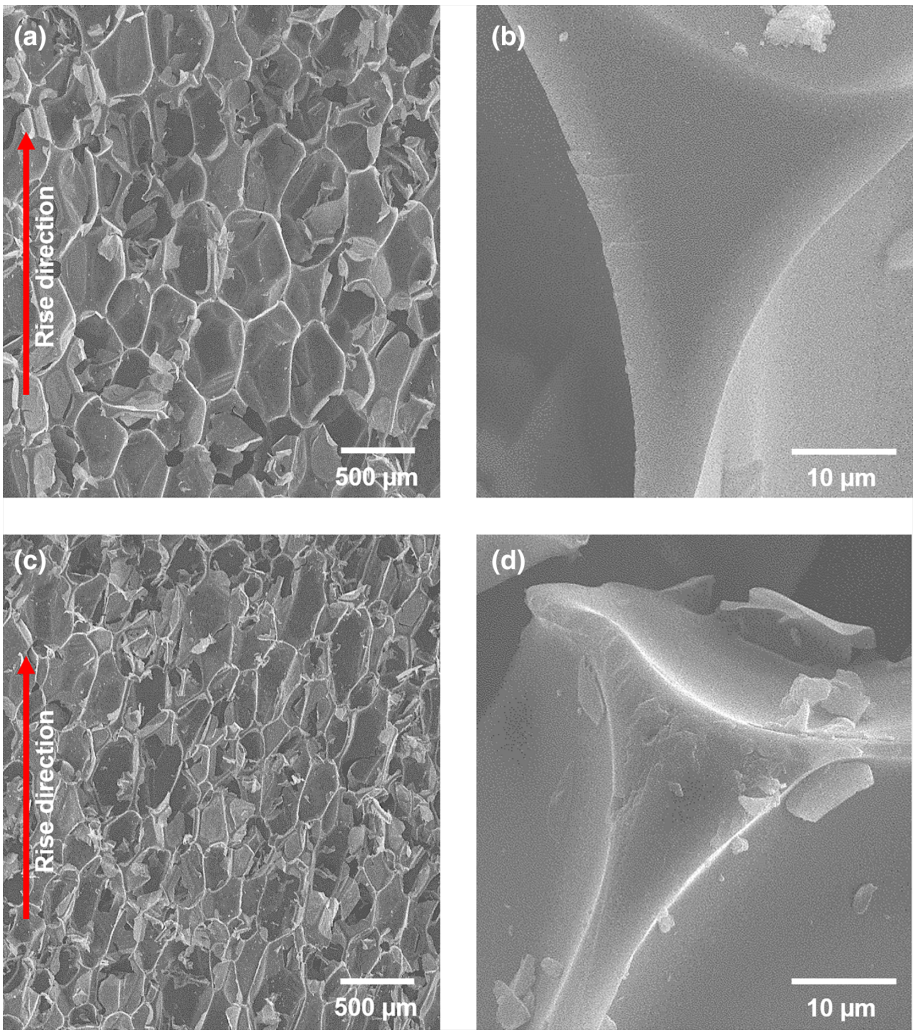

Figure 3. SEM images of (a) PUF cells; (b) cross section of single strut of PUF; (c) BNCF cells; (d) cross section of single strut of BNCF. [Color figure can be viewed at wileyonlinelibrary.com]

and the other to the point with the minimum gradient on the plateau or strain hardening part.[67] The densification strain was determined using the method based on the maximum of energy absorption efficiency curve.[68] In this method, the energy efficiency $\eta(\varepsilon)$ is defined as:

$$\eta(\varepsilon) = \frac{1}{\sigma(\epsilon)} \int_0^{\epsilon} \sigma(\epsilon) d\epsilon \quad (1)$$

where $\sigma(\varepsilon)$ and ε are the engineering stress and engineering strain, respectively. The maximum of the energy absorption efficiency corresponds to the densification strain.

Notwithstanding that both PUF and BNCF have similar density, the PUF has a yield stress ~15% higher than that of the BNCF in the longitudinal direction (Figure 4) for quasi-static loading. For the transverse direction, the yield stress of PUF is 55% higher than that of the BNCF. This indicates that adding BNC into the microstructure of the foam resulted in a decrease of the yield stress. This could be explained by a reduction of the cell wall thickness as a consequence of the cell size reduction in the BNCF, when the relative density is similar to that of the PUF. It has been reported for PUFs that the effect of cell size reduction on foam compressive strength is usually negative.[69,70] The reduction of yield stress in the BNCF could also be explained by the slight deviation of cell orientation (~10–15°) with respect to the foam rise direction [Figure 3(c)]. It has also been reported for PUFs that there is a decrease in yield stress with the increase of the angle between the cell orientation and the foam rise direction due to anisotropy.[67] Although this effect might be considered as a drawback, the reduction of the yield stress in the BNCF may be considered as an advantage from a design viewpoint of FGFs given that these results show that the mechanical properties of RPUFs can potentially be tailored using different types of nanoreinforcements so as to absorb energy at different rates without changing the density of the material. A numerical study of FGFs is presented in the next section.

Figure 4 also shows the strain-rate effects on the yield stress and densification strain. For the PUF in the longitudinal direction, increases of around 10 and 25% are observed for the yield stress for strain rates of 0.016 and 150 s^{-1}, respectively, when compared to the quasi-static yield stress. It is noted that the difference between the quasi-static strain rate and 0.016 s^{-1} is one order of

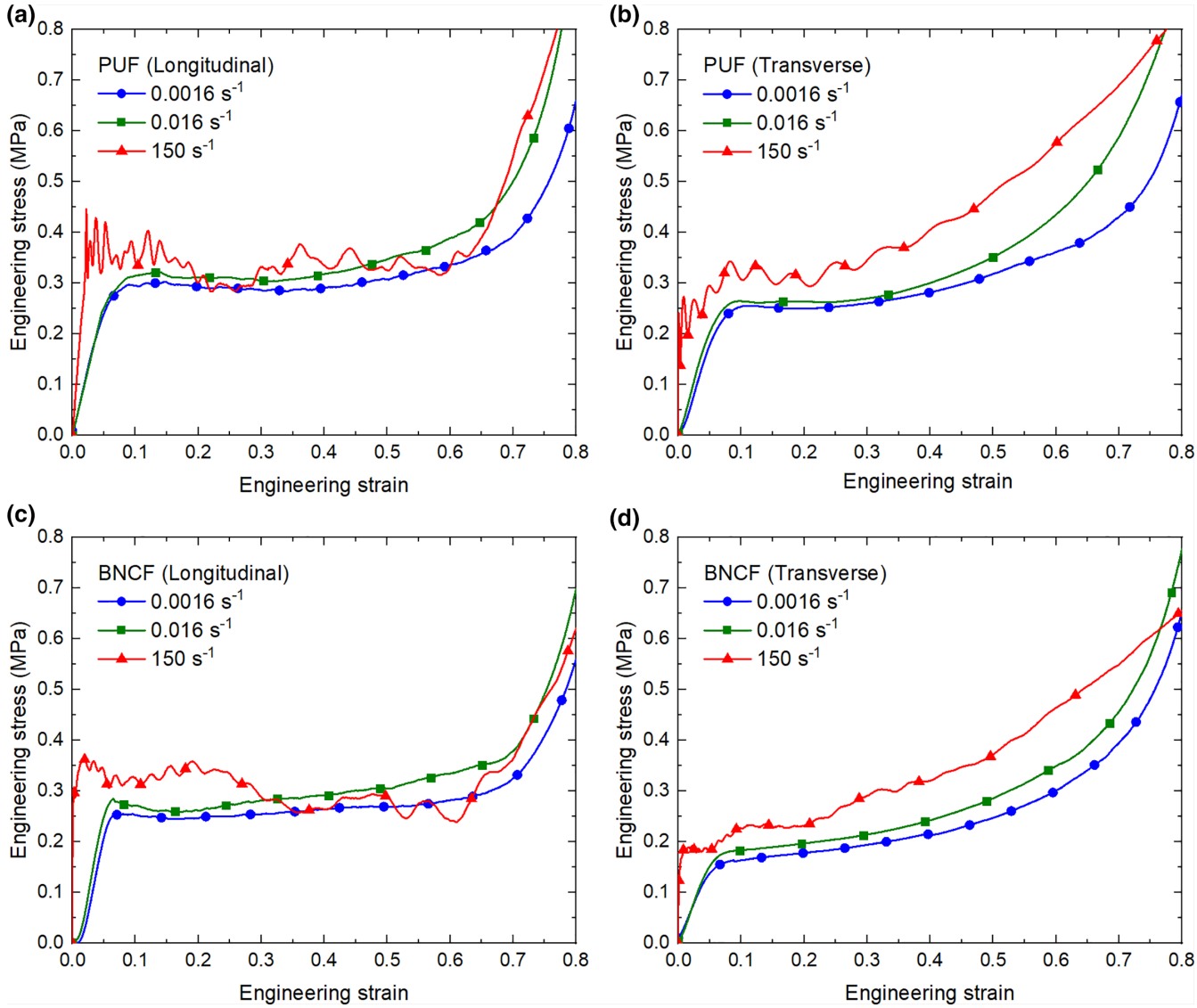

Figure 4. Compressive stress–strain curves at different strain rates and loading directions: (a) PUF in the longitudinal direction, (b) PUF in the transverse direction, (c) BNCF in the longitudinal direction, and (d) BNCF in the transverse direction. [Color figure can be viewed at wileyonlinelibrary.com]

magnitude while the difference between 0.016 and 150 s^{-1} is nearly four orders of magnitude. Therefore, a larger increase in yield stress will be produced when the strain rate increases from 0.016 to 150 s^{-1} when compared to an increase from quasi-static strain rate to 0.016 s^{-1}. The strain rate effect is primarily associated with the strain rate sensitivity of the base polymer material from which the foam is made and the entrapped air in the closed cells, which is compressed locally and increases the material rate sensitivity.[43] For PUF in the transverse direction, the increases for those strain rates (0.016 and 150 s^{-1}) are 5 and 25%, respectively. For BNCF, increases in the yield stress of around 10 and 35% are observed, respectively, for both directions. There was no significant strain-rate effect on the elastic modulus and yield strain. It is noted that the elastic modulus and yield strain could not be measured accurately from the dynamic compression curves (150 s^{-1}). The strain-rate effect on densification strain is not significant when the strain rate increases from 0.0016 to 0.016 s^{-1} in all cases; however, a reduction of around 10% is observed when the strain rate increases from 0.0016 to 150 s^{-1} for both PUF and BNCF in the longitudinal direction. This may be explained by the entrapped gas effect on polymer foams.[71] It is noted that the densification strain could not be measured accurately in the transverse direction from the dynamic compression curves for both foams. It can also be seen in Figure 4(a,c) that there is a drop in the engineering stress at around 0.6 engineering strain for the PUF and BNCF, respectively, in the longitudinal direction for a strain rate of 150 s^{-1}. The drop is more pronounced in the BNCF [Figure 4(c)]. This behavior may be explained by a reduction of the strain rate at large strains due to the deceleration of the impactor during foam compression,[63] which in turn results in a reduction of the stress level. It is noted that this behavior is not observed in the transverse direction, which may be explained by the lower yield stress of both foams in this direction.

Table I. Measured Mechanical Properties of PUF and BNCF

Material	PUF (longitudinal)			PUF (transverse)			BNCF (longitudinal)			BNCF (transverse)		
Strain rate (s^{-1})	16×10^{-3}	16×10^{-2}	15×10^{2}	16×10^{-3}	16×10^{-2}	15×10^{2}	16×10^{-3}	16×10^{-2}	15×10^{2}	16×10^{-3}	16×10^{-2}	15×10^{2}
E (MPa)	5.4	5.5	—	4.2	4.3	—	6.2	6.5	—	3.2	3.2	—
σ_y (MPa)	0.29	0.32	0.37	0.26	0.27	0.32	0.25	0.28	0.35	0.16	0.18	0.21
ε_y (%)	5.8	5.8	—	6.4	6.2	—	5.5	5.4	—	5.2	5.2	—
ε_d (%)	0.66	0.64	0.60	0.68	0.62	—	0.68	0.67	0.61	0.63	0.62	—

Figure 5(a,b) shows the deformation process of PUF subjected to compression at different times t of dynamic loading (150 s^{-1}) in the longitudinal and transverse directions, respectively. It can be seen that the PUF exhibits localized progressive crushing [Figure 5 (a), (t) = 0.004 s] in the longitudinal direction while uniform deformation is observed in the transverse direction [Figure 5(b), (t) = 0.004 s). This is explained by the fact that in the longitudinal direction, the main plastic deformation mechanism is the buckling of cell struts aligned with the loading direction while in the transverse direction, the main mechanism is the flexure of cell struts.[67] Figure 6(a,b) shows the deformation process of BNCF subjected to compression at different times t of dynamic loading (150 s^{-1}) in the longitudinal and transverse directions, respectively. Similar to the PUF, the BNCF exhibits localized progressive crushing in the longitudinal direction [Figure 6(a), (t) = 0.004 s]. However, in the transverse direction, the BNCF also exhibits localized progressive crushing [Figure 6(b), (t) = 0.004 s) and a remarkable recovery [Figure 6(b), t = 0.04 s] when compared to the PUF in the same direction. It is believed that the incorporation of BNC into the foam changed the deformation and energy absorbing mechanisms, reducing significantly its friability. These results may be explained by the measured nucleation effect that BNC has on the PUF.

NUMERICAL SIMULATIONS OF FGF

FE Modeling

FE simulations of FGF subjected to low velocity impact were performed using Abaqus/Explicit (Version 2016).[72] Numerical simulation was employed as a tool to understand the effect of using layers with the same density but different compressive strengths in the direction of load, in a multilayered foam block subjected to impact. FE simulations have been successfully used along with experimental work to study the dynamic behavior of rigid foams[73,74] and FGF.[75,76] For this numerical study, a three-layer foam block, in which, each layer has the same density but different stress–strain responses, is modeled. The experimental curves of PUF in the longitudinal direction and BNCF in the transverse direction were utilized as the input stress–strain response for the model. The geometry of the multilayered foam block was $25 \times 25 \times 25$ mm^3. The foam block model was built as a three-dimensional solid and consisted of three layers of $25 \times 25 \times 8.33$ mm^3, as shown in Figure 7. A perfect bond between layer interfaces was assumed and modeled using the tie constraint option.[77] The mesh comprises linear hexahedral elements (C3D8). The impactor and base plate were modeled as rigid bodies. A total of 15,625 elements were used for the foam block with an average element size of 1 mm^3. A mesh sensitivity analysis showed that this level of mesh refinement was deemed sufficient for our numerical model. A finer mesh was also tested, which did not show any significant variation in the load response, but a significant increase in computational time. Contact between the foam specimen and steel parts was modeled using finite sliding formulation and surface-to-surface contact. A penalty friction formulation was used for tangential contact behavior with a coefficient of friction of 0.2.

Materials Properties

The base plate and impactor were modeled using an available isotropic elastic material model with following material properties: Young's modulus E = 210 GPa, Poisson's ratio ν = 0.3, and density

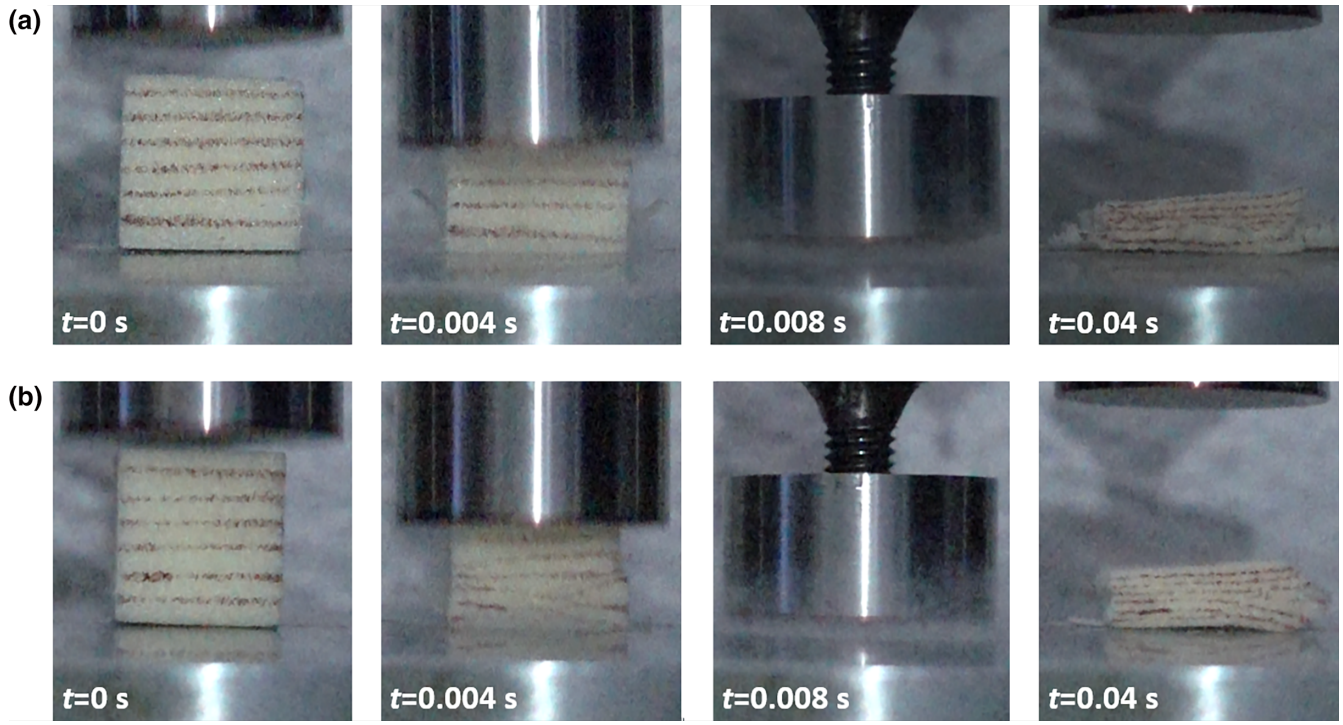

Figure 5. Deformation process of PUF compressed at a strain rate of 150 s^{-1}: (a) longitudinal direction and (b) transverse direction. [Color figure can be viewed at wileyonlinelibrary.com]

ρ = 7800 kg m^{-3}. The elastic behavior of the foam block was modeled using the uniaxial compression elastic modulus from Table I, ν = 0 and density of 40 kg m^{-3}. The plastic behavior was modeled using the crushable foam material model with following parameters: compression yield stress ratio k = 1 and hydrostatic yield stress ratio k_t = 0.1. These values were chosen because the

Figure 6. Deformation process of BNCF compressed at a strain rate of 150 s^{-1}: (a) longitudinal direction and (b) transverse direction. [Color figure can be viewed at wileyonlinelibrary.com]

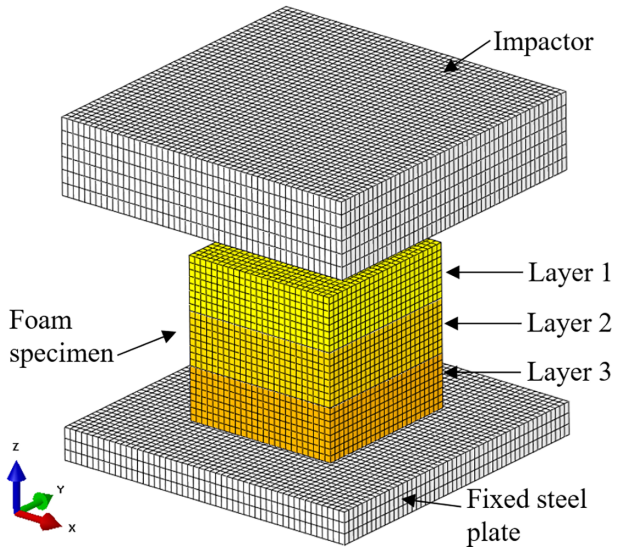

Figure 7. FE mesh of multilayered FGF block subjected to low velocity impact. [Color figure can be viewed at wileyonlinelibrary.com]

material response of the foam block is mainly dominated by compressive stress.[78] For the crushable foam hardening tabular data, experimental curves from uniaxial quasi-static compression test were used (Figure 4). The strain-rate dependence of strength was modeled using the rate dependence hardening option with yield ratio option. The yield ratio R is defined as $R = \bar{\sigma}/\sigma_0$, where $\bar{\sigma}$ and σ_0 are the yield stress at nonzero strain rate and the quasi-static yield stress, respectively.[72] R can be obtained from the values of σ_y in Table I and entered directly as a tabular function of the axial plastic strain rate for the crushable foam model.[72] To simulate impact loading on the foam block, the steel impactor had an initial impact velocity of 3.7 m s^{-1} and a mass of 1.6 kg.

Numerical Results

Figure 8(a,b) shows the numerical results from compression tests for PUF in the longitudinal direction and BNCF in the transverse direction, respectively, at three different strain rates. Quasi-static (0.0016 s^{-1}) experimental results are also included in Figure 8 as a reference. A good agreement between the numerical simulation and the experimental result for uniaxial quasi-static compressive test is observed for up to ~50% strain. Figure 8 also shows the predicted stress–strain curves for strain rates of 0.016 and 150 s^{-1}, which are in good agreement with the strength observed experimentally [Figure 4(a,d)]. Since we are interested in using the numerical simulations to better understand the energy absorption rate of the FGF before the densification regime, the model employed here was deemed sufficient for our simulation results.

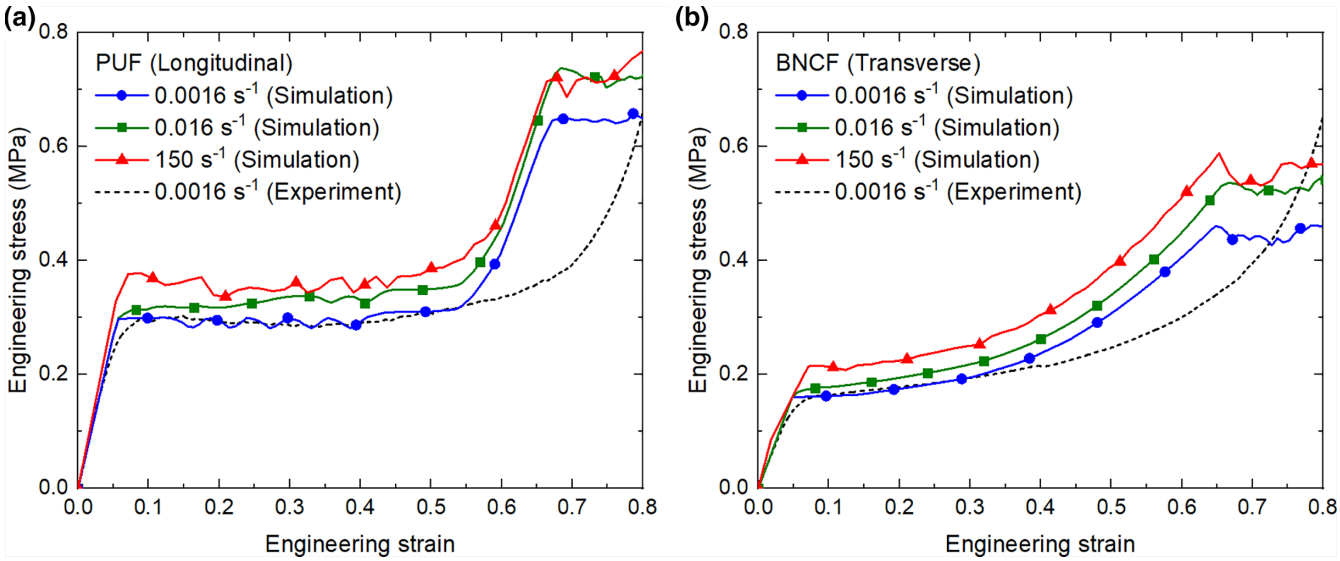

Figure 8. Predicted compressive stress–strain curves at three different strain rates: (a) PUF in the longitudinal direction, (b) BNCF in the transverse direction. Experimental quasi-static stress–strain curves are included as a reference. [Color figure can be viewed at wileyonlinelibrary.com]

Table II. Eight Selected Cases to Investigate the Effect of Using Layers with the Same Density but Different Mechanical Properties on FGF Blocks

Case	Case 1 (PPP)	Case 2 (PBP)	Case 3 (PPB)	Case 4 (BPP)	Case 5 (BPB)	Case 6 (BBP)	Case 7 (PBB)	Case 8 (BBB)
Layer	Material							
Layer 1 (top)	PUF	PUF	PUF	BNCF	BNCF	BNCF	PUF	BNCF
Layer 2 (middle)	PUF	BNCF	PUF	PUF	PUF	BNCF	BNCF	BNCF
Layer 3 (bottom)	PUF	PUF	BNCF	PUF	BNCF	PUF	BNCF	BNCF

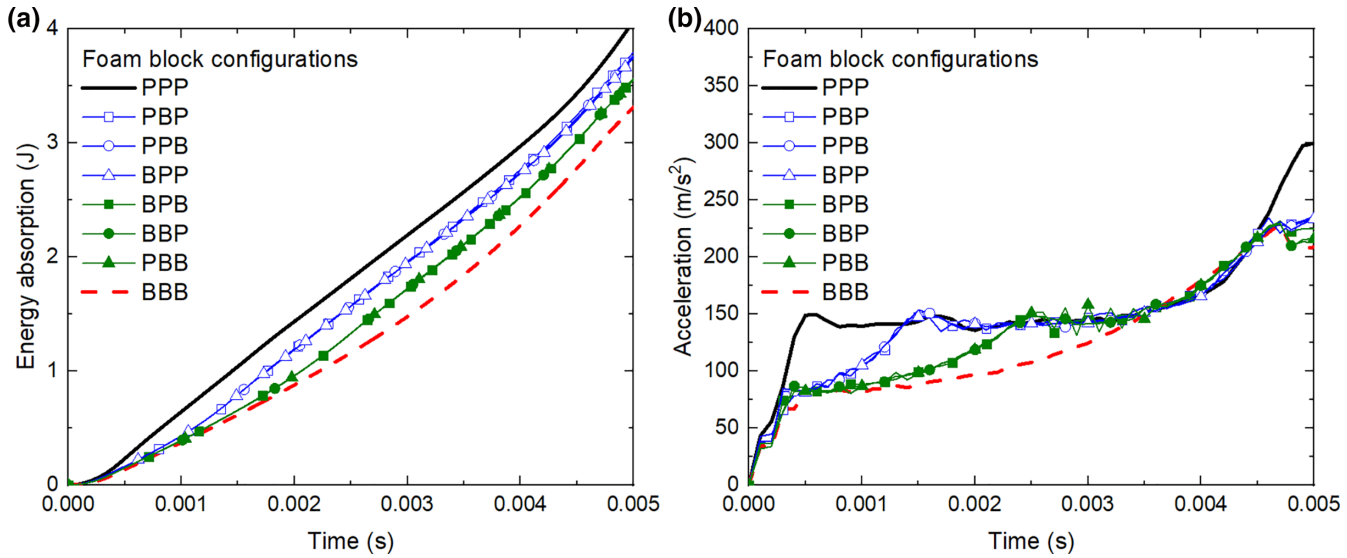

Figure 9. Predicted time-history plots of (a) energy absorption and (b) acceleration for different FGF block configurations (Cases 1–8 in Table II). [Color figure can be viewed at wileyonlinelibrary.com]

The FGF block configurations used in this study are shown in Table II. Two different sets of material properties were used as input material parameters for the layers, that is, the material properties of PUF in the longitudinal direction (Material P) and material properties of BNCF in the transverse direction (Material B). Eight different cases were evaluated as shown in Table II to investigate the effect of using layers of foam with the same density but different mechanical properties.

Figure 9(a) shows time-history plots of the energy absorption (absorbed energy) for all FGF block configurations. It can be seen that the PPP foam block (Case 1) exhibits the highest energy absorption rate (absorbed energy per unit time) while the BBB foam block (Case 8) exhibits the lowest energy absorption rate, as expected. Cases 2–4 exhibit the same energy absorption rate, which indicates that the energy absorption rate for these cases depends on the overall stiffness and plastic behavior of the foam block rather than the material layering. Cases 5–7 also exhibit a similar energy absorption rate, which is lower than that of Cases 2–4. Figure 9(b) shows acceleration-time history curves of the impactor for different FGF block configurations (Table II). It can be seen

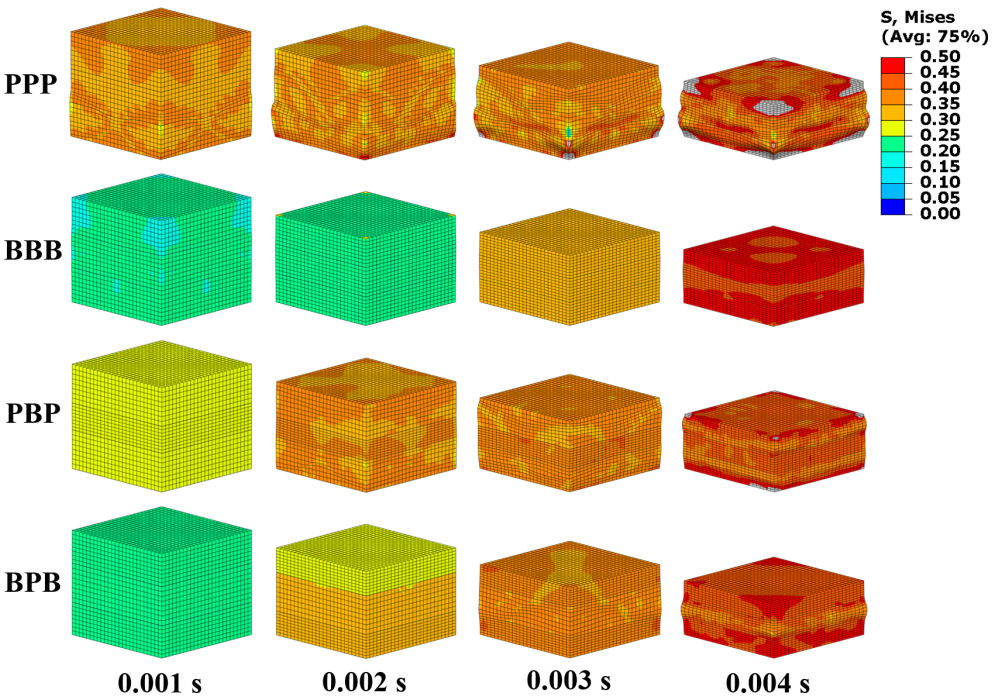

Figure 10. Contour plots of von Mises stress for four different cases of FGF block configurations at different times of dynamic loading. [Color figure can be viewed at wileyonlinelibrary.com]

that the PPP foam block (Case 1) produces that highest acceleration rate while the BBB foam block (Case 8) produces the lowest acceleration rate. Cases 2–7 produce acceleration rates that are between that of Cases 1 and 8. Figure 10 shows contour plots of von Mises stress for four different cases of FGF block configurations at different times of dynamic loading in the numerical simulations. Contour plots are displayed based on average values at nodes common to two or more elements when the contributing elements lie in the same result region.[72] The averaging threshold value of 75% (Figure 10) means that if the relative nodal variation for each node included in the plot is less than 75%, values of contributing elements are averaged at that node. This produces a smooth and continuous effect in the display of the results with few noticeable discontinuities from element to element. It can be seen in Figure 10 that for Case 1 (PPP) localized crushing is observed while for Case 8 (BBB) uniform deformation is observed. For Case 2 (PBP), the initial crushing occurs mainly in the middle layer with low stiffness. This is also observed for Case 5 (BPB), in which the crushing starts at the external layers with low stiffness.

The numerical results show that a FGF block can be designed using different layers of PUF and BNCF with the same density but different mechanical properties, to vary the energy absorption and acceleration rates during low velocity impact. These results are important from a design viewpoint because PUFs properties, such as stiffness and strength, can potentially be tailored using BNC to absorb energy at different rates for impact applications using foam layers with the same density. The FE simulations presented here could be used to predict impact response of FGFs in more complex geometries.

CONCLUSIONS

In this work, rigid PUFs nanostructured with BNCF at 0.2 wt % and without it (PUF) were synthesized. SEM images showed that, for the BNCF, a substantial cell size decrease was observed in both longitudinal (rise) direction and transverse direction when compared to the PUF. This indicates that the BNC acted as a nucleation agent; however, the measured apparent density of BNCF and PUF was similar ($\sim$40 kg m^{-3}), which shows that the incorporation of BNC resulted in cell size reduction while maintaining a similar apparent density. Compression test at different strain rates (0.0016, 0.016, and 150 s^{-1}) were performed on foam specimens in both directions. For both PUF and BNCF, the yield stress was higher in the longitudinal direction when compared to the transverse direction, which is associated with the anisotropy of the foams. Both PUF and BNCF exhibited strain-rate effect on yield stress and densification strain, which is primarily associated with the strain-rate sensitivity of the base polymer material from which the foam is made and the entrapped air in the closed cells. A reduction of the yield stress was observed for the BNCF in both directions when compared to the PUF, which is associated with the cell size reduction caused by the BNC. This reduction of the yield stress may be considered as an advantage from a design viewpoint of FGFs because these results show that the mechanical properties of RPUFs can potentially be tailored using nanoreinforcement to absorb energy at different rates. Images of the dynamic compression test showed that in the transverse direction, the BNCF exhibits localized progressive crushing and a remarkable recovery when compared to the PUF. It is believed that the incorporation of BNC into the foam changed the deformation and energy absorbing mechanisms, significantly reducing its friability. FE simulations of FGF subjected to low velocity impact were performed using Abaqus/Explicit code to understand the effect of using layers with the same density but different compressive strengths in the direction of loading. The numerical simulations showed that FGF blocks can be designed using different layers of PUF and BNCF with the same density to vary the energy absorption and acceleration rates during low velocity impact. The numerical approach employed here could be extended to predict the impact response in more complex geometries. However, the numerical results in this study are limited and further research has to be carried out to fully understand this type of FGF. The mechanical results presented herein warrant further research of nanostructured RPUFs to reveal the mechanisms that modify the mechanical properties of nanostructures foams for impact applications. It is concluded that nanostructured RPUFs are a noteworthy option for protective structures subjected to impact as they may potentially lead to weight-savings and improvement in the energy-absorption performance and energy absorption rate of the structure. Further research should include the effect of BNC concentration on the dynamic mechanical properties of RPUFs and numerical simulations of FGF with more than three layers and different stacking configurations.

ACKNOWLEDGMENTS

This work was supported by the Agencia Nacional de Promoción Científica y Tecnológica (ANPCyT) through the project PICT-2015-N0475 and Cátedras CONACYT (Cátedras Project 1241). The authors thank the technical support from Francisco Koh with the drop-weight impact tower, Santiago Duarte Aranda for the SEM images, and Matías Nonna for providing the polyurethane systems.

REFERENCES

1. Tuwair, H.; Hopkins, M.; Volz, J.; ElGawady, M. A.; Mohamed, M.; Chandrashekhara, K.; Birman, V. *Compos. Part B*. **2015**, *79*, 262.
2. Chiacchiarelli, L. Biomass, Biopolymer-Based Materials, and Bioenergy; Elsevier: Swaston, Cambridge, **2019**.
3. Briscoe, C. R.; Mantell, S. C.; Davidson, J. H.; Okazaki, T. *J. Sandwich Struct. Mater.* **2011**, *13*, 23.
4. La Rosa, A.; Recca, A.; Gagliano, A.; Summerscales, J.; Latteri, A.; Cozzo, G.; Cicala, G. *Construct. Build Mater.* **2014**, *55*, 406.
5. Lu, G.; Yu, T. Energy Absorption of Structures and Materials; Elsevier: Cambridge, England, **2003**.
6. Paulino, M.; Teixeira-Dias, F. Polyurethane; InTech: London, UK, **2012**.
7. Szycher, M. Szycher's Handbook of Polyurethanes; Taylor & Francis group LLC: Florida, NY, **2013**.
8. Mills, N. J.; Fitzgerald, C.; Gilchrist, A.; Verdejo, R. *Compos. Sci. Technol.* **2003**, *63*, 2389.
9. Demirel, S.; Ergun Tuna, B. *Polym. Test.* **2019**, *76*, 146.

10. Lee, D.-J.; Kim, M.-K.; Walsh, J.; Jang, H.-K.; Kim, H.-I.; Oh, E.-Y.; Nam, J.; Kim, M.; Suhr, J. *Polym. Test.* **2019**, *74*, 30.
11. Randall, D.; Lee, S. The Polyurethanes Book; Wiley: Hoboken, NJ, **2003**.
12. Ashida, K. Polyurethane and Related Foams: Chemistry and Technology; CRC Press: Boca Raton, **2006**.
13. Jordan, J.; Jacob, K. I.; Tannenbaum, R.; Sharaf, M. A.; Jasiuk, I. *Mater. Sci. Eng. A*. **2005**, *393*, 1.
14. Hussain, F.; Hojjati, M.; Okamoto, M.; Gorga, R. E. *J. Compos. Mater.* **2006**, *40*, 1511.
15. Zou, H.; Wu, S. S.; Shen, J. *Chem. Rev.* **2008**, *108*, 3893.
16. Güleç, F.; Sher, F.; Karaduman, A. *Pet. Sci.* **2019**, *16*, 161.
17. Zarren, G.; Nisar, B.; Sher, F. *Mater. Today Sustainability*. **2019**, *5*, 100019.
18. Sher, F.; Sajid, Z.; Tokay, B.; Khzouz, M.; Sadiq, H. *Asia-Pac. J. Chem. Eng.* **2016**, *11*, 855.
19. Cordero, A. I.; Amalvy, J. I.; Fortunati, E.; Kenny, J. M.; Chiacchiarelli, L. M. *Carbohydr. Polym.* **2015**, *134*, 110.
20. Gimenez, R. B.; Leonardi, L.; Cerrutti, P.; Amalvy, J.; Chiacchiarelli, L. M. *J. Appl. Polym. Sci.* **2017**, *134*, 44982.
21. Septevani, A. A.; Evans, D. A.; Annamalai, P. K.; Martin, D. J. *Ind. Crops Prod.* **2017**, *107*, 114.
22. Chang, L.-C.; Sain, M.; Kortschot, M. *J. Cell. Plast.* **2015**, *51*, 103.
23. Lobos, J.; Velankar, S. *J. Cell. Plast.* **2016**, *52*, 57.
24. Faruk, O.; Sain, M.; Farnood, R.; Pan, Y.; Xiao, H. *J. Polym. Environ.* **2014**, *22*, 279.
25. Dolomanova, V.; Rauhe, J. C. M.; Jensen, L. R.; Pyrz, R.; Timmons, A. B. *J. Cell. Plast.* **2011**, *47*, 81.
26. Lee, L. J.; Zeng, C.; Cao, X.; Han, X.; Shen, J.; Xu, G. *Compos. Sci. Technol.* **2005**, *65*, 2344.
27. Charreau, H.; L Foresti, M.; Vázquez, A. *Recent Pat. Nanotechnol.* **2013**, *7*, 56.
28. Foresti, M.; Cerrutti, P. Vazquez, A. In Polymer Nanocomposites Based on Inorganic and Organic Nanomaterials; Mohanty, S. K. N.; Kaith, B.; Kalia, S., Eds., John Wiley & Sons, Inc: Hoboken, NJ, **2015**.
29. Herrán, R.; Amalvy, J. I.; Chiacchiarelli, L. M. *J. Appl. Polym. Sci.* **2019**, 47959.
30. Shin, S. R.; Kim, H. N.; Liang, J. Y.; Lee, S. H.; Lee, D. S. *J. Appl. Polym. Sci*. **2019**, 47916.
31. Kim, J.-H.; Shim, B. S.; Kim, H. S.; Lee, Y.-J.; Min, S.-K.; Jang, D.; Abas, Z.; Kim, J. *Int. J. Precis. Eng. Manuf. Technol.* **2015**, *2*, 197.
32. Chirayil, C. J.; Mathew, L.; Thomas, S. *Rev. Adv. Mater. Sci.* **2014**, *37*, 20.
33. Kurańska, M.; Barczewski, M.; Uram, K.; Lewandowski, K.; Prociak, A.; Michałowski, S. *Polym. Test.* **2019**, *76*, 90.
34. Kadam, H.; Bandyopadhyay-Ghosh, S.; Malik, N.; Ghosh, S. B. *J. Appl. Polym. Sci.* **2019**, *136*, 47063.
35. Hinckley, W. M.; Yang, J. *Exp. Mech.* **1975**, *15*, 177.
36. Sherwood, J. A.; Frost, C. C. *Polym. Eng. Sci.* **1992**, *32*, 1138.
37. Jeong, K. Y.; Cheon, S. S.; Munshi, M. B. *J. Mech. Sci. Technol.* **2012**, *26*, 2033.
38. Chen, W.; Lu, F.; Winfree, N. *Exp. Mech.* **2002**, *42*, 65.
39. Sadighi, M.; Salami, S. J. *Cent. Eur. J. Eng.* **2012**, *2*, 627.
40. Jung, A.; Beex, L. A. A.; Diebels, S.; Bordas, S. P. A. *Mater. Des.* **2015**, *87*, 36.
41. Henry, F.; Williamson, C. In 11th International Conference on the Packaging and Transportation of Radioactive Materials (PATRAM'95), **1995**; p 1161.
42. Sun, Y.; Li, Q. M. *Int. J. Impact Eng.* **2018**, *112*, 74.
43. Ouellet, S.; Cronin, D.; Worswick, M. *Polym. Test.* **2006**, *25*, 731.
44. Uddin, M. F.; Mahfuz, H.; Zainuddin, S.; Jeelani, S. In Proceedings of the 6th International Symposium on MEMS and Nanotechnology, **2005**; p 147.
45. Mohammed, A. A.; Hosur, M.; Jeelani, S. *Cell. Polym.* **2006**, *25*, 293.
46. Nasirzadeh, R.; Sabet, A. R. *J. Cell. Plast.* **2014**, *52*, 253.
47. Luo, H.; Zhang, Y.; Wang, B.; Lu, H. *J. Offshore Mech. Arct. Eng.* **2010**, *132*, 021301.
48. Park, S.-B.; Choi, S.-W.; Kim, J.-H.; Bang, C.-S.; Lee, J.-M. *Compos. Part B*. **2016**, *93*, 317.
49. Pellegrino, A.; Tagarielli, V.; Gerlach, R.; Petrinic, N. *Int. J. Impact Eng.* **2015**, *75*, 214.
50. Sachse, S.; Poruri, M.; Silva, F.; Michalowski, S.; Pielichowski, K.; Njuguna, J. *J. Sandwich Struct. Mater.* **2014**, *16*, 173.
51. Hosur, M.; Mohammed, A.; Zainuddin, S.; Jeelani, S. *Compos. Struct.* **2008**, *82*, 101.
52. Hosur, M.; Mohammed, A.; Zainuddin, S.; Jeelani, S. *Mater. Sci. Eng. A*. **2008**, *498*, 100.
53. Bhuiyan, M. A.; Hosur, M. V.; Jeelani, S. *Compos. Part B*. **2009**, *40*, 561.
54. Reis, P. N. B.; Santos, P.; Ferreira, J. A. M.; Richardson, M. O. W. *J. Reinf. Plast. Compos.* **2013**, *32*, 898.
55. Kargarzadeh, H.; Huang, J.; Lin, N.; Ahmad, I.; Mariano, M.; Dufresne, A.; Thomas, S.; Gałęski, A. *Prog. Polym. Sci.* **2018**, *87*, 197.
56. de Campos, A.; Corrêa, A. C.; Claro, P. I. C.; de Morais Teixeira, E.; Marconcini, J. M. In Sustainable Polymer Composites and Nanocomposites; Inamuddin; Thomas, S.; Kumar Mishra, R.; Asiri, A. M., Eds., Springer International Publishing: Cham, **2019**.
57. Pinto, E. R. P.; Barud, H. S.; Polito, W. L.; Ribeiro, S. J. L.; Messaddeq, Y. *J. Therm. Anal. Calorim.* **2013**, *114*, 549.
58. Seydibeyoğlu, M. Ö.; Misra, M.; Mohanty, A.; Blaker, J. J.; Lee, K.-Y.; Bismarck, A.; Kazemizadeh, M. *J. Mater. Sci.* **2013**, *48*, 2167.
59. Singh, S. N. Blowing Agents for Polyurethane Foams; Rapra Technology: Shawbury, UK, **2001**.
60. Kenny, J. M.; Torre, L.; Chiacchiarelli, L. M. *J. Appl. Polym. Sci.* **2015**, *132*, 110.

61. Zimmermann, M. V. G.; da Silva, M. P.; Zattera, A. J.; Campomanes Santana, R. M. *J. Appl. Polym. Sci.* **2017**, *134*, 44760.
62. Flores-Johnson, E. A.; Li, Q. M. *J. Cell. Plast.* **2011**, *47*, 45.
63. Ramirez, B. J.; Kingstedt, O. T.; Crum, R.; Gamez, C.; Gupta, V. *J. Appl. Phys.* **2017**, *121*, 225107.
64. Cao, X.; James Lee, L.; Widya, T.; Macosko, C. *Polymer*. **2005**, *46*, 775.
65. Flores-Johnson, E. A.; Li, Q. M.; Mines, R. A. W. *J. Cell. Plast.* **2008**, *44*, 415.
66. Tu, Z. H.; Shim, V. P. W.; Lim, C. T. *Int. J. Solids Struct.* **2001**, *38*, 9267.
67. Li, P.; Guo, Y. B.; Zhou, M. W.; Shim, V. P. W. *Int. J. Impact Eng.* **2019**, *127*, 154.
68. Flores-Johnson, E. A.; Li, Q. M. *Int. J. Solids Struct.* **2010**, *47*, 1987.
69. Kabakci, E.; Sayer, G.; Suvaci, E.; Uysal, O.; Güler, İ.; Kaya, M. *J. Appl. Polym. Sci.* **2017**, *134*, 44870.
70. Smits, G. F. *J. Therm. Insul. Build. Envelopes*. **1994**, *17*, 309.
71. Sun, Y.; Li, Q. M. *Int. J. Solids Struct.* **2015**, *63*, 50.
72. ABAQUS. Abaqus Analysis User's Guide, version 2016. In Dassault Systèmes: Providence, **2015**.
73. Flores-Johnson, E. A.; Li, Q. M.; Shen, L. *Int. J. Comput. Methods*. **2014**, *11*, 1344004.
74. Whisler, D.; Kim, H. *Polym. Test.* **2015**, *41*, 219.
75. Zhang, X.; Zhang, H. *Int. J. Mech. Sci.* **2013**, *68*, 199.
76. Cui, L.; Forero Rueda, M. A.; Gilchrist, M. D. *Mater. Des.* **2009**, *30*, 3414.
77. Vázquez-Rodríguez, J. M.; Flores-Johnson, E. A.; Herrera-Franco, P. J.; Gonzalez-Chi, P. I. *Polym. Compos.* **2018**, *39*, E2397.
78. Flores-Johnson, E. A.; Li, Q. M. *Compos. Struct.* **2012**, *94*, 1555.